



Carbon quantum dots as nano-scaffolds for α -Fe₂O₃ growth: Preparation of Ti/CQD@ α -Fe₂O₃ photoanode for water splitting under visible light irradiation

Omran Moradlou^{a,*}, Zeinab Rabiei^a, Alireza Banazadeh^b, Juliusz Warzywoda^c, Mohammad Zirak^d

^a Department of Chemistry, Alzahra University, P.O. Box: 1993893973, Tehran, Iran

^b Department of Chemistry and Biochemistry, Texas Tech University, Lubbock, TX, USA

^c Materials Characterization Center, Whitacre College of Engineering, Texas Tech University, Lubbock, TX 79409-3103, USA

^d Department of Physics, Hakim Sabzevari University, P.O. Box 961797648, Sabzevar, Iran

ARTICLE INFO

Keywords:

Hematite

CQD

Nanostructuring

Water splitting

ABSTRACT

To improve the photoresponsivity of hematite-based photoanode via better charge transfer rate and short paths for the electron transport, carbon quantum dots (CQDs) were used as conductive nano-scaffolds for the growth of photoactive material on Ti substrate. CQDs@ α -Fe₂O₃ nanoparticulates with the average diameter of 3–5 nm were uniformly grown on the substrate under the finely optimized experimental conditions to prepare Ti/CQDs@ α -Fe₂O₃ photoanode. The photocurrent response of the resulted photoanode with a photocurrent density of 2.1 mA cm⁻² at applied E_{bias} of +0.5 V vs. Ag/AgCl was increased by a factor of 10 compared to Ti/ α -Fe₂O₃, mainly due to the improvement in charge-transfer rate and suppression of electron-hole recombination derived from the increased hole-diffusion length in conducting nano-scaffold structure. The surface morphology of samples was investigated with FE-SEM and HRTEM. Charge transfer resistance (R_{ct}) of Ti/ α -Fe₂O₃ and Ti/CQDs@ α -Fe₂O₃ photoanodes were estimated to be about 90.9 and 3.7 K Ω , respectively. After the continuous 4 h illumination of Ti/CQDs@ α -Fe₂O₃ photoanode under the visible light irradiation, the efficiency of water splitting process (i.e. the photocurrent) did not changed significantly (\pm 5%), indicating the high stability of photoanode and tightly deposited CQDs@ α -Fe₂O₃ on Ti substrate, which was confirmed by FE-SEM image of the sample after the experiment. The formation of carbon-oxygen chemical bonds between CQDs and hematite molecules was confirmed by X-ray photoelectron spectroscopy (XPS). Finally, based on XRD pattern and photoresponses of various photoanodes annealed at different temperatures, the results showed that the structure design is as significant as crystallinity in hematite-based photoelectrodes.

1. Introduction

Hematite, α -Fe₂O₃, has been identified as an excellent semiconductor material for the fabrication of photoanodes in photoelectrochemical (PEC) water splitting processes because of its good chemical and photoelectrochemical stability, earth-abundance, low cost, environmental friendliness and having a narrow energy band gap (E_g) of about 2.2 eV with the valence band edge position below the water oxidation potential [1]. Increasing PEC efficiency of hematite-based photoanodes remains a challenge and a large body of research has been carried out to solve its limitations [2]. The main drawbacks of hematite as a photoactive semiconductor are the short hole-diffusion length (a few nanometers without bias and tens of nanometers with bias), poor hole mobility (0.01 cm² V⁻¹ s⁻¹) and hole lifetime, high overvoltage

(i.e. slow kinetics) of the oxygen evolution reaction and the electron-hole recombination [3]. Among these problems, the short hole-diffusion length within hematite is an important limiting factor [4].

Several strategies have been developed to address these limitations including: (a) doping the elements (Ti, Nb, Mo, Si, etc.) to introduce additional mobile charge carriers [2,5]; (b) introducing intermediate layer at hematite/substrate interface to enhance the hole transport; (c) introducing water oxidation catalyst such as cobalt-phosphate (Co-Pi) [6–8] and IrO_x [9] on hematite film to accelerate water oxidation kinetics; (d) passivating the surface trapping states of hematite with overlayer deposition with Al₂O₃ [10], Fe₂TiO₅ [3], Ytterbium [11] or heterojunctions to reduce the surface electron-hole recombination; and finally, (e) control of crystallinity [12] and (f) morphology [13] of hematite.

* Corresponding author.

E-mail address: moradlou@alzahra.ac.ir (O. Moradlou).

It is believed that the deposition of highly crystalline hematite on the substrate is the best way to enhance the charge separation [12–14]. In fact, the surface trapping states are believed to present on the hematite films and the energetic traps could be a result of a disordered crystalline surface [15]. However, even in single crystal hematite films, the short hole-diffusion length within hematite remains unsolved. So, the control of hematite morphology is seems to be important. In this respect, to achieve a balance between light harvesting and hole collection, the overall photoactive material morphology should be kept in nanoscale. Vertically aligned nanorods [16] and worm-like structure [12,17] are two ideal morphologies for PEC applications of α -Fe₂O₃. Nanorods can overcome hole transport limitations, because their lateral dimensions matches the short hole-diffusion length and the photo-excited electrons could flow through a direct pathway along the axial direction of rods [18]. Because of the same reason, high photocurrent densities can also be achieved from worm-like hematite [12,17] as well as hematite quantum dots with the size of few nanometers grown on α -Fe₂O₃ nanorods [19]. As a drawback for the nanoscale morphology, nanostructuring offers longer paths for the electron transport to the conductive substrate and increases the probability of electron-hole recombination [13].

So, an appropriate approach would be the synthesis of crystalline hematite with the nanostructured morphology having a reasonable conductivity, better charge transfer rate and short paths for the electron transport. Base on this idea, this work aims the use of carbon quantum dots (CQDs) as nano-scaffolds for the growth of α -Fe₂O₃ on conductive substrate under the finely optimized experimental conditions.

2. Experimental

2.1. Fabrication of Ti/ α -Fe₂O₃ and Ti/CQD@ α -Fe₂O₃ photoanode

All chemicals were of analytical grade and deionized water (DI water, 18 M Ω) was used throughout the work. The electrochemical method was used for the synthesis of CQDs as reported elsewhere [20] by using two graphite rods (as anode and cathode) immersed in a 100 mL solution of ethanol:H₂O (99:1) containing 0.30 g NaOH under the applied constant current intensity of 180 mA cm⁻² for 24 h. The obtained soluble CQDs were then separated by silica-gel column chromatography with an appropriate developing solvent (a mixture of 1:1 petroleum ether:diethyl ether) after the treatment with MgSO₄ [20]. For comparison, CQDs were also synthesized under the applied constant current intensities of 100 and 20 mA cm⁻².

For the fabrication of Ti/CQD@ α -Fe₂O₃ photoanode, hydrothermal method was used. Typically, in an aqueous solution of 0.1 mg mL⁻¹ CQD (10.0 mL), an appropriate amounts of Fe³⁺ (0.05 M) and NaNO₃ (1.0 M) were added and the pH of solution was adjusted to 1.40 (by adding H₂O:HCl (10:1, v/v) solution) and stirred for 15 min. The mixture was then transferred to a highly cleaned 50-mL Teflon-lined stainless steel autoclave, and a pre-cleaned Ti sheet (3 \times 1 cm²) was immersed vertically into the solution and heated to 100 °C for 6 h. Ti substrate which was coated with yellow-orange thin film of CQD@ α -Fe₂O₃ was annealed at 390 °C for 1 h. For the fabrication of Ti/ α -Fe₂O₃ using hydrothermal method, the same procedure was used where the CQD solution was replaced with DI water.

Ti/ α -Fe₂O₃ thin films were also fabricated by depositing iron oxy-hydroxide (FeOOH) using successive ion layer adsorption and reaction (SILAR) process and then annealing in air at 500 °C. For the fabrication of Ti/ α -Fe₂O₃, two separate aqueous solutions of Fe³⁺ (0.05 M) and NaOH (0.1 M) were prepared. Then, pre-cleaned Ti substrates were immersed into these two separate solutions for 20 s each. Between each immersion step, the samples were rinsed with DI water. Different number of immersion cycles (10, 20, 30, 50, 100 and 150 cycles) was considered as well. Ti substrates which were coated with a thin film of iron hydroxide were annealed at 390 °C, 500 °C or 600 °C for 1 h and denoted as Ti/ α -Fe₂O₃-n samples, where n is the cycle number.

2.2. Photoelectrochemical measurements

The photoresponse was investigated in a three-electrode electrochemical cell with a Ti/ α -Fe₂O₃, Ti/ α -Fe₂O₃-n or Ti/CQD@ α -Fe₂O₃ photoanode as working electrode, a platinum plate as a counter electrode and an Ag/AgCl (KCl 3.0 M) as a reference electrode. The electrochemical measurements were carried out using a Galvanostat/Potentiostat Autolab PGSTAT101 instrument. The electrochemical impedance spectroscopy (EIS) of the samples was studied by Autolab PGSTAT 302N equipped with FRA Impedance Module. The light power spectrum (a Xenon arc lamp coupled with a UV cut-off filter ($\lambda_{\text{off}} < 400$ nm), 100 mW cm⁻²) was measured with a common photocell [21]. During all PEC measurements, 1.0 M KOH was used as electrolyte.

2.3. Instruments and photoanode characterization

The morphology of the prepared photoanodes was observed with field emission-scanning electron microscopy (FE-SEM, EM3900M, ZEISS, Germany) equipped with EDAX energy dispersive X-ray spectrometer (EDS) for inspecting the elemental composition of the samples. Transmission electron microscopy (TEM, Philips), and high resolution transmission electron microscopy (HRTEM, Hitachi H-9500 transmission electron microscope) were used for size and morphology studies, selected area electron diffraction (SAED) analysis and HRTEM imaging of the nanostructures. The surface chemical composition of the synthesized samples was characterized by X-ray photoelectron spectroscopy (XPS, PHI 5000 Versa Probe). The XPS data were collected in an ultra-high vacuum chamber equipped with a monochromatic Al-K α X-ray (1486.6 eV). All binding energies (E_b) in XPS spectra were calibrated by fixing C(1s) core level line at E_b = 285.0 eV. SDP software (version 4.1) was used to analyze XPS peak deconvolutions, after a Shirley background subtraction. To study the crystal phase of samples, X-ray diffraction (PW1800, Philips) with CoK α radiation (λ = 1.78 Å) was used. In order to study the absorption spectra of samples (to calculate the E_g), UV–vis diffuse reflectance spectroscopy (Avantes, Avaspec 2048) was used. BaSO₄ was applied as a reflectance standard in DRS experiments.

3. Results and discussion

The characterization of Ti/ α -Fe₂O₃ and Ti/CQD@ α -Fe₂O₃ photoanodes including their surface morphology, crystal phase and energy band gaps (E_g) was investigated. Ti/ α -Fe₂O₃ photoanodes were fabricated by using two methods, i.e. hydrothermal method and successive ion layer adsorption and reaction (SILAR) process. In hydrothermal reaction method, the effects of main experimental conditions including Fe³⁺ precursor concentration and reaction time were studied. In this respect, six Ti/ α -Fe₂O₃ samples were prepared according to the conditions included in Table 1. SILAR process was also employed for the fabrication of different six Ti/ α -Fe₂O₃-n samples as described in experimental section. The main reason for the fabrication of Ti/ α -Fe₂O₃-n samples with SILAR method (where n is the cycle number of SILAR process) is to study the effect of α -Fe₂O₃ thin film thickness on their photoactivity. SILAR is a solution-based layer-by-layer deposition method that provides tight control over the film thickness. It should be noted that in all comparative studies between the photoresponsivity of Ti/ α -Fe₂O₃ and Ti/CQD@ α -Fe₂O₃ photoanodes, the results of hydrothermally prepared Ti/ α -Fe₂O₃ electrodes have been reported.

After the fabrication of all samples, their morphology, crystal phase and energy band gaps (E_g) were studied. Finally, the photoactivity of all samples was investigated using various electrochemical methods including chronoamperometry, chronopotentiometry and electrochemical impedance spectroscopy (EIS).

Table 1

The experimental conditions for the fabrication of six Ti/ α -Fe₂O₃ samples by using hydrothermal method and their corresponding photocurrent densities (J_{ph} , mA cm⁻²).

Sample	Fe ³⁺ precursor concentration (M)	Hydrothermal reaction time (h)	Average film thickness (μ m)	J_{ph} (mA cm ⁻²)
Ti/ α -Fe ₂ O ₃ -L6h	5.0×10^{-2}	6.0	0.10	0.80
Ti/ α -Fe ₂ O ₃ -H6h	1.5×10^{-1}	6.0	1.50	0.20
Ti/ α -Fe ₂ O ₃ -L12h	5.0×10^{-2}	12.0	1.40	0.40
Ti/ α -Fe ₂ O ₃ -H12h	1.5×10^{-1}	12.0	~5	0.10
Ti/ α -Fe ₂ O ₃ -L24h	5.0×10^{-2}	24.0	~5	0.30
Ti/ α -Fe ₂ O ₃ -H24h	1.5×10^{-1}	24.0	~6	0.20

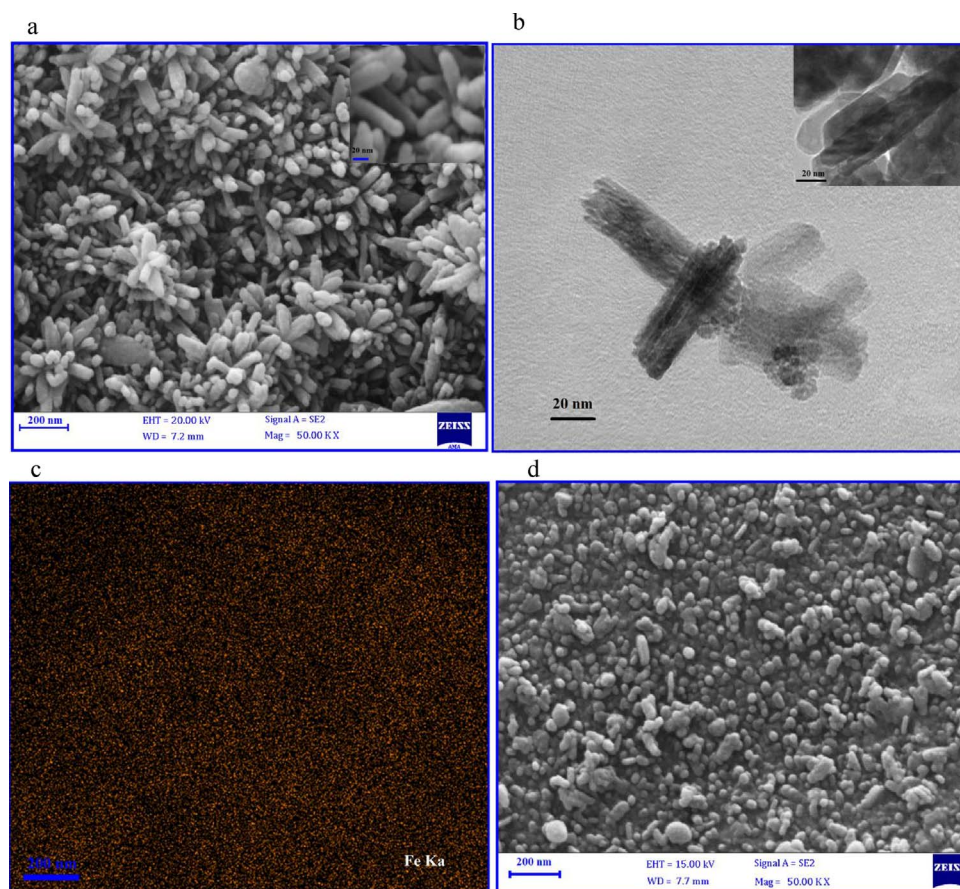


Fig. 1. (a) FE-SEM image of α -Fe₂O₃ nanorods grown on Ti substrate by hydrothermal method (Ti/ α -Fe₂O₃-L6h sample). (b) HRTEM image of α -Fe₂O₃ nanorods of Ti/ α -Fe₂O₃-L6h. (c) FE-SEM mapping image of Fe in Ti/ α -Fe₂O₃-L6h sample. The experimental conditions for the fabrication of Ti/ α -Fe₂O₃-L6h sample were: Fe³⁺ precursor concentration of 0.05 M, NaNO₃ concentration of 1.0 M, hydrothermal reaction temperature of 100°C and reaction time of 6 h. (d) FE-SEM image of Ti/ α -Fe₂O₃-100 prepared by SILAR method.

3.1. Morphology of Ti/ α -Fe₂O₃ and Ti/CQD@ α -Fe₂O₃ photoanodes

Morphology of the prepared Ti/ α -Fe₂O₃ and Ti/CQD@ α -Fe₂O₃ samples was investigated using FE-SEM and HRTEM. Six Ti/ α -Fe₂O₃ samples were prepared by using hydrothermal method at different Fe³⁺ precursor concentrations and the hydrothermal reaction times (Table 1). Fig. 1a shows the FE-SEM image of Ti/ α -Fe₂O₃-L6h sample prepared under the experimental conditions including Fe³⁺ precursor concentration of 0.05 M and the hydrothermal reaction time of 6 h. As it is clear, the morphology of hydrothermally prepared α -Fe₂O₃ is 1-D nanorod. In addition, by increase in Fe³⁺ precursor concentration or hydrothermal reaction time, the average diameter of α -Fe₂O₃ 1-D nanorods and their length, and consequently, the thickness of α -Fe₂O₃ thin film on Ti substrate is increased (Supplementary Materials, Fig. S1, Table 1). HRTEM images of α -Fe₂O₃ samples were also investigated. Fig. 1b shows the TEM image of Ti/ α -Fe₂O₃-L6h sample. The average diameter of α -Fe₂O₃ nanorods is about 25 nm and their average length is about 200 nm, confirming the FE-SEM results. The SEM-EDS map of the sample (Fig. 1c) shows the uniform distribution of Fe element on Ti substrate.

However, the morphology of Ti/ α -Fe₂O₃ samples prepared by

SILAR method (Ti/ α -Fe₂O₃-n) is nanoparticles uniformly covered the surface of Ti substrate (Fig. 1d) and certainly does not have the nanorod structure that was resulted from the hydrothermal deposition method. The difference in the morphology of Ti/ α -Fe₂O₃ photoanodes fabricated by two methods raises from the preferred growth mechanism of hematite prepared under the different experimental conditions. It seems that the hydrothermal synthesis of α -Fe₂O₃ nanorods follows two stages including the initial nucleation of rod-like akaganeite nuclei [22] and the subsequent ripening of nuclei together to form akaganeite (β -FeOOH) nanorods would then transform to hematite (α -Fe₂O₃) nanorods by annealing. On the other hand, in the synthesis of Ti/ α -Fe₂O₃-n samples by SILAR method, the morphology of the as-deposited iron oxide thin film is nanoparticle with the average grain size of about 30 nm.

As discussed, the main aim of this work is the heterojunction construction of CQD@ α -Fe₂O₃ photoactive materials on conductive Ti substrate to study the effect of CQDs on the photoresponsivity of Ti/CQD@ α -Fe₂O₃. So, after the synthesis of CQDs with the electrochemical method, the hydrothermal reaction at mild conditions (Section 2.1) was used to fabricate yellow-orange thin film of CQD@ α -Fe₂O₃ on Ti substrate.

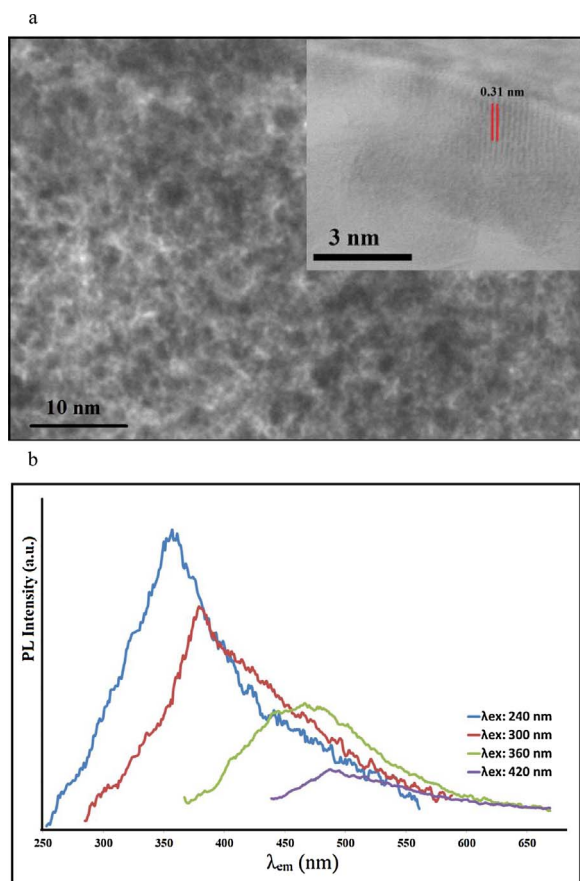


Fig. 2. (a) HRTEM image of CQDs. (b) PL spectra of electrochemically synthesized CQDs at various excitation wavelengths of 240, 300, 360 and 420 nm.

The electrochemically synthesized CQDs were characterized with HRTEM and photoluminescence (PL) spectroscopy. Fig. 2a shows high-resolution TEM image of CQDs with the average diameter of 2.0 nm with the lattice spacing of around 0.31 nm, which agrees well with $\langle 002 \rangle$ spacing of graphitic carbon [20,23,24]. To investigate the optical properties of as-synthesized CQDs, the study was carried out by using different excitation wavelengths (λ_{ex}) of 240, 300, 360 and 420 nm (Fig. 2b). As it is clear, CQDs give visible light emission in the range of 300–600 nm. This is the same result as reported for CQDs with the sizes in the range of 1.5–3.0 nm [20]. Also, by varying the λ_{ex} , the wavelength of PL with maximum intensity (λ_{em}) shifts to the longer wavelengths (Red shift), which is the characteristics optical properties of CQDs.

The surface morphology of the fabricated Ti/CQD@ α -Fe₂O₃ photoanode was characterized with FE-SEM (Fig. 3a) and SEM mapping (Fig. 3b and c). The FE-SEM-EDS map of the sample (Fig. 3b and c) shows the uniform distribution of Fe and C elements on Ti substrate. The FE-SEM image confirmed that the morphology of CQD@ α -Fe₂O₃ is quite different from that of α -Fe₂O₃ grown by hydrothermal method under the same experimental conditions except the presence of CQDs in the reaction solution in CQD@ α -Fe₂O₃. To confirm the FE-SEM results, morphology of CQD@ α -Fe₂O₃ was examined with HRTEM (Fig. 3d and e). The HRTEM images clearly show the nanoparticles of CQD@ α -Fe₂O₃ in which CQDs act as core for the growth of α -Fe₂O₃ shell. It seems that in the presence of CQDs in hydrothermal reaction solution, the growth mechanism of α -Fe₂O₃ nanoparticles is quite different from that of α -Fe₂O₃ nanorods grown on Ti in the absence of CQDs. In fact, CQDs with the average size of 2 nm act as nano-scaffolds to form uniform CQDs@ α -Fe₂O₃ nanoparticles on the substrate. So, it can be concluded that CQDs can serve as the nucleation sites for the growth of FeOOH nuclei around CQDs resulting CQD@ α -Fe₂O₃ nanoparticles

with the average size of 3–5 nm. To confirm this growth mechanism, CQDs@ α -Fe₂O₃ nanostructures were grown on Ti substrate with higher concentrations of Fe³⁺ precursor (0.15 M) or at longer hydrothermal reaction time (12 h). The morphology of the resulted sample was examined by HRTEM, as shown in Fig. 3f. As it is clear from TEM image, among the growth of CQD@ α -Fe₂O₃ nanoparticulates, α -Fe₂O₃ nanorods were also grown adjacent to the nanoparticulates, confirming the important role of CQDs in the formation of specific morphology. From the selected area electron diffraction (SAED) pattern of α -Fe₂O₃ at CQD@ α -Fe₂O₃ nanoparticulates (Fig. 3g), the spacing values of the lattice fringes were determined to be 3.624, 2.657 and 2.173 Å, which can be indexed to hematite α -Fe₂O₃ [25,26].

3.2. Crystal phase and spectroscopic characterizations of photoanodes

The typical XRD patterns of α -Fe₂O₃ and CQD@ α -Fe₂O₃ nanocomposites are shown in Fig. 4a. XRD patterns of α -Fe₂O₃ prepared by two different methods (hydrothermal and SILAR methods) were the same. The characteristic diffraction peaks for α -Fe₂O₃ and CQD@ α -Fe₂O₃ samples were observed at 2θ values of 24.1019°, 33.0966°, 35.6004°, 40.8064°, 49.4007°, 53.9896°, 57.4886°, 62.3551° and 63.9145°, attributed to (012), (104), (110), (113), (024), (116), (122), (214) and (300) crystal planes, respectively. This result is consistent with the HRTEM and SAED analyses. All diffraction peaks can be indexed to the rhombohedral hematite (JPCDS 00-024-0072). The sharp peaks for these samples confirm the high crystallinity of the photoactive materials. The diffraction peaks of CQD@ α -Fe₂O₃ nanocomposite match well with α -Fe₂O₃, while the peaks in CQD@ α -Fe₂O₃ nanocomposite widened and the peak intensities suppressed, indicating the influence of CQDs on crystallinity and crystallite size of hematite. This finding supports the FESEM and HRTEM results and the differences observed in the morphology of α -Fe₂O₃ and CQD@ α -Fe₂O₃.

Band gap energy (E_g) of the hydrothermally fabricated photoanodes were calculated from diffuse reflectance spectral (DRS) data (Fig. 4b) and plot of $(\alpha h\nu)^2$ vs. photon energy ($h\nu$) (Fig. 4c) based on the Kubelka–Munk function ($\alpha h\nu = A(h\nu - E_g)^n$). E_g 's of Ti/ α -Fe₂O₃ and Ti/CQD@ α -Fe₂O₃ samples were obtained to be 2.10 eV and 2.05 eV, respectively. It means that CQDs has no effect on the band gap energy of hematite-based nanocomposites.

The surface chemical composition of the synthesized samples was characterized by X-ray photoelectron spectroscopy (XPS). Full XPS spectrum (survey spectrum) of CQD@ α -Fe₂O₃ surface has been shown in Fig. 5. The presence of main elements of Fe, O and C is obvious in XPS survey spectrum. As it is clear, the Fe and O related peaks have significant higher intensity than C 1s peak. This is an evidence that CQDs have been covered by Fe₂O₃ shell and is in agreement with HRTEM images of the sample (Fig. 3e). High resolution XPS scans (XPS windows) of Fe 2p core level (Fig. 5b) shows two distinct peaks with binding energies (BE) of 723.3 and 710.1 eV, which are assigned to Fe 2p_{1/2} and Fe 2p_{3/2} energy levels, respectively [27–30]. The observed BE difference between these two peaks is 13.2 eV arising from the spin-orbit splitting effect. A weak satellite Fe³⁺ peak is also observed at 718 eV. These peaks are ascribed to 3+ oxidation state of Fe, verifying the formation of α -Fe₂O₃ stoichiometry [28,29]. Fig. 5c shows XPS window of C 1s core level. This spectrum exhibits two main peaks centered at 285 (named as A) and 290 eV (named as B), which are attributed to carbon–carbon and carbon–oxygen bonds, respectively [27–29,31–33]. The A peak has been deconvoluted to two peaks with BE of 285.0 and 286.3 eV which are attributed to C–C and C=C bonds of CQDs, respectively [27,29,32]. The peak B has been curve fitted by two peaks located at BE values of 289.4 and 290.6 eV which are assigned to C–O and C=O bonds, respectively [27,29,32]. The presence of B peak (carbon–oxygen bonds) with remarkable intensity as compared to A peak (carbon–carbon bonds), revealed that the chemical bonds exist between C atoms of CQDs and O atoms of hematite, similar to XPS spectrum of C 1s for iron carbonate [33]. Chemical bond

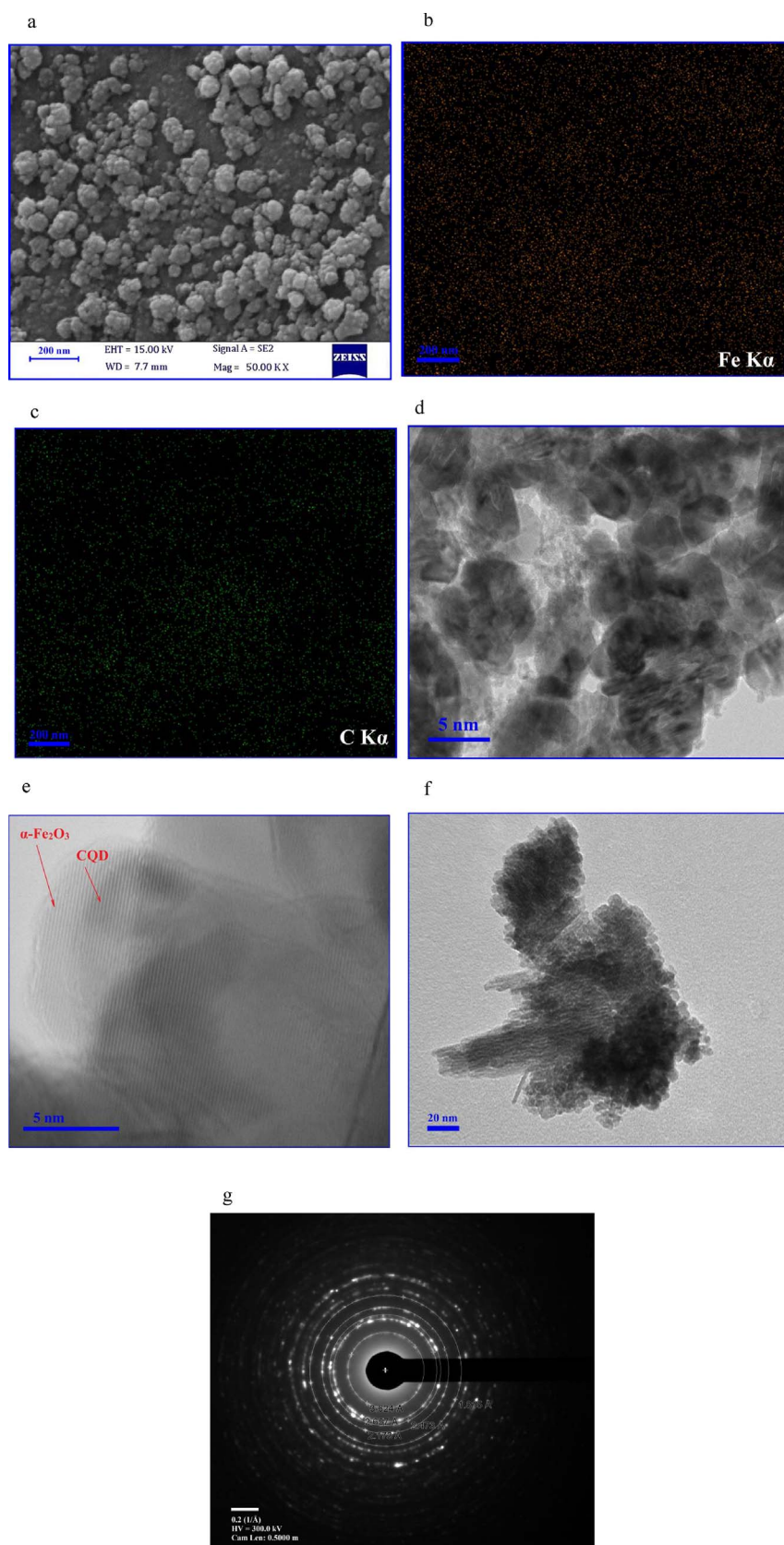


Fig. 3. (a) FE-SEM image (top view) from Ti/CQD@ α -Fe $_2$ O $_3$ photoanode fabricated by hydrothermal method. (b and c) FE-SEM mapping image of Fe (b) and carbon (c) in Ti/CQD@ α -Fe $_2$ O $_3$ sample. (d and e) HRTEM image of CQD@ α -Fe $_2$ O $_3$ nanoparticles at different magnifications. (f) HRTEM image of CQD@ α -Fe $_2$ O $_3$ synthesized at Fe $^{3+}$ precursor concentration of 0.15 M, NaNO $_3$ concentration of 1.0 M, hydrothermal reaction temperature of 100 °C and reaction time of 12 h. (g) Selected area electron diffraction (SAED) pattern of α -Fe $_2$ O $_3$ in CQD@ α -Fe $_2$ O $_3$.

formation between hematite and CQDs molecules can also be verified through investigation of O 1s XPS window (Fig. 5d). As Fig. 5d shows, O 1s spectrum has been deconvoluted to 4 peaks with BE of 530.1, 531.8, 533.3 and 536.8 eV. These peaks are ascribed to O $^{2-}$ bonds with Fe,

C=O, O–C=O and H $_2$ O (physically adsorbed) related bonds, respectively [27–29,31–33]. It is also obvious that the oxygen-carbon bonds have noticeable contribution in O 1s spectrum. Therefore, O 1s XPS window curve fitting confirmed again the formation of carbon-oxygen

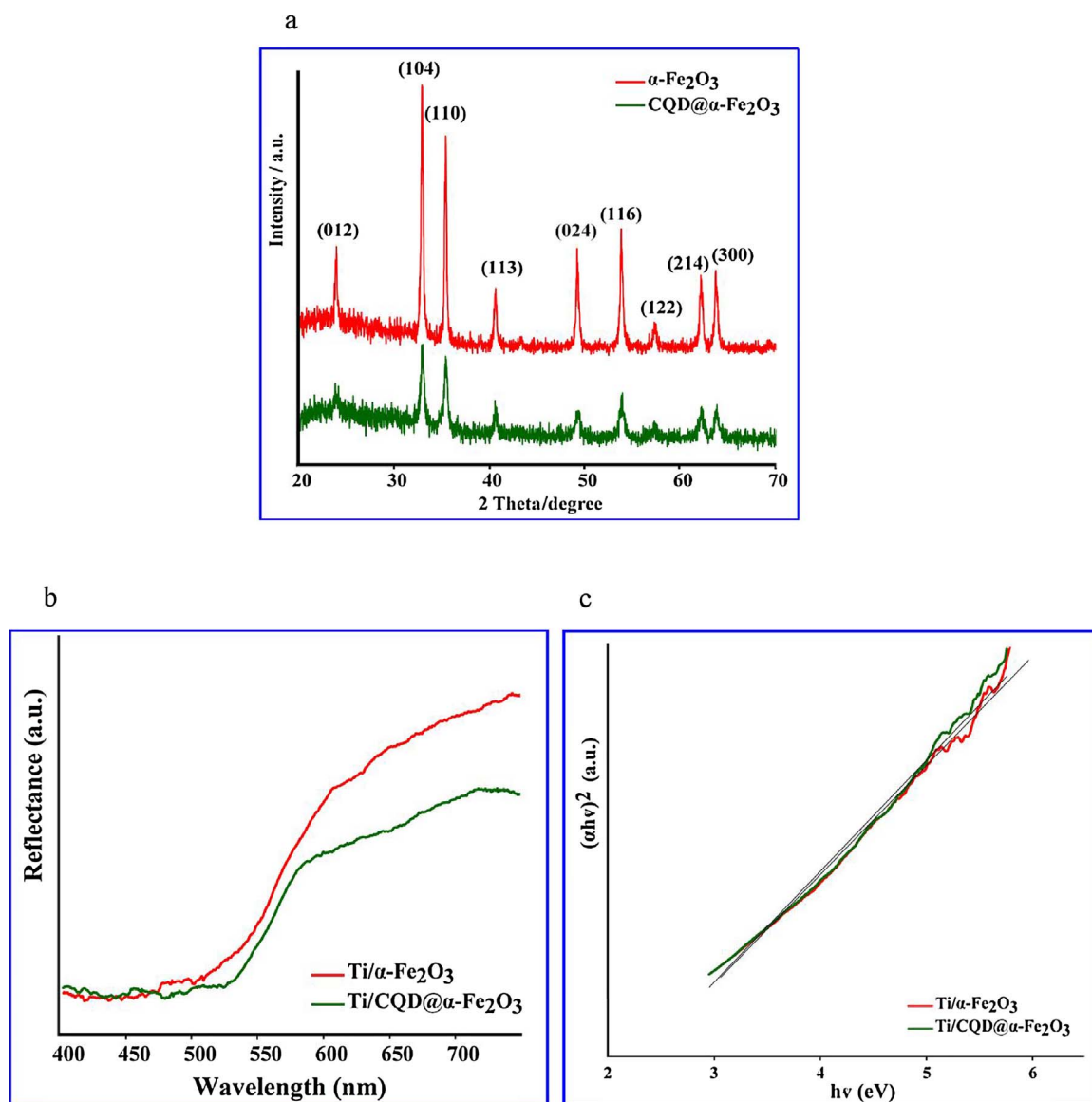


Fig. 4. (a) XRD patterns of $\alpha\text{-Fe}_2\text{O}_3$ and $\text{CQD}@ \alpha\text{-Fe}_2\text{O}_3$. (b) Diffuse reflectance spectra (DRS) of $\text{Ti}/\alpha\text{-Fe}_2\text{O}_3$ and $\text{Ti}/\text{CQD}@ \alpha\text{-Fe}_2\text{O}_3$ photoanodes. (c) Plot of $(\alpha h\nu)^2$ vs. photon energy ($h\nu$, eV) of photoanodes.

chemical bonds.

3.3. Electrochemical performance of photoanodes

3.3.1. Linear sweep voltammetry

Linear sweep voltammetry (LSV) was used to investigate the onset potential of water oxidation and photoactivity of samples. The photocurrent densities ($J_{\text{ph}}/\text{mA cm}^{-2}$) of $\text{Ti}/\alpha\text{-Fe}_2\text{O}_3$ and $\text{Ti}/\text{CQD}@ \alpha\text{-Fe}_2\text{O}_3$ photoelectrodes were measured in both dark and illuminating conditions as a function of applied bias from 0 to 1.0 V (Fig. 6a). Under dark conditions, the onset water oxidation potential occurs at 0.80 V and 0.65 V at the $\text{Ti}/\alpha\text{-Fe}_2\text{O}_3$ and $\text{Ti}/\text{CQD}@ \alpha\text{-Fe}_2\text{O}_3$ electrode surfaces, respectively. A distinguished 150 mV cathodic shift of onset potential at $\text{Ti}/\text{CQD}@ \alpha\text{-Fe}_2\text{O}_3$ electrode surface indicates the lower overpotential toward water oxidation, i.e. the faster water oxidation kinetics at the surface of electrode. This is probably due to the higher conductivity of the $\text{CQD}@ \alpha\text{-Fe}_2\text{O}_3$ thin film compared with $\alpha\text{-Fe}_2\text{O}_3$ [34] and improved charge transfer in nanostructured $\text{CQD}@ \alpha\text{-Fe}_2\text{O}_3$ [35]. Under the visible light irradiation, the electron-hole pairs are generated at the surface of both photoanodes when the applied bias is reached to the onset potential of about 0.25 V (Fig. 6a). The obtained onset potential

under the visible light irradiation is lower than or comparable with the previously reported $\alpha\text{-Fe}_2\text{O}_3$ -based photoanodes (Table 2).

It means that the overpotential of water oxidation on the electrode surface is low and the kinetics of water oxidation is faster. Under the illumination conditions, the measured J_{ph} for $\text{Ti}/\text{CQD}@ \alpha\text{-Fe}_2\text{O}_3$ photoanode as a function of applied potential (J_{ph} vs. E_{bias}) at different illumination intensities (I_{light}) were also depicted in Fig. 6b. The photocurrent density (J_{ph}) of the $\text{Ti}/\text{CQD}@ \alpha\text{-Fe}_2\text{O}_3$ photoanode was increased with the increase of incident light intensity. In order to understand the relationship between the generated J_{ph} and the applied illumination intensity (I_{light}), a diagram of J_{ph} versus I_{light} was drawn at 0.5 V potential (Fig. 6c). A linear relationship between J_{ph} and I_{light} has been obtained suggesting that the charge carriers (e^-h^+ pair) generation is a dominant phenomenon in the water splitting reaction under visible illumination [47].

3.3.2. Electrochemical impedance spectroscopy

It is implied from the LSV of $\text{Ti}/\text{CQD}@ \alpha\text{-Fe}_2\text{O}_3$ photoanode that CQDs may improve the charge transfer in nanostructured $\text{CQD}@ \alpha\text{-Fe}_2\text{O}_3$. In order to get more insight into the charge transfer resistances (R_{ct}) of $\text{Ti}/\alpha\text{-Fe}_2\text{O}_3$ and $\text{Ti}/\text{CQD}@ \alpha\text{-Fe}_2\text{O}_3$ photoanodes,

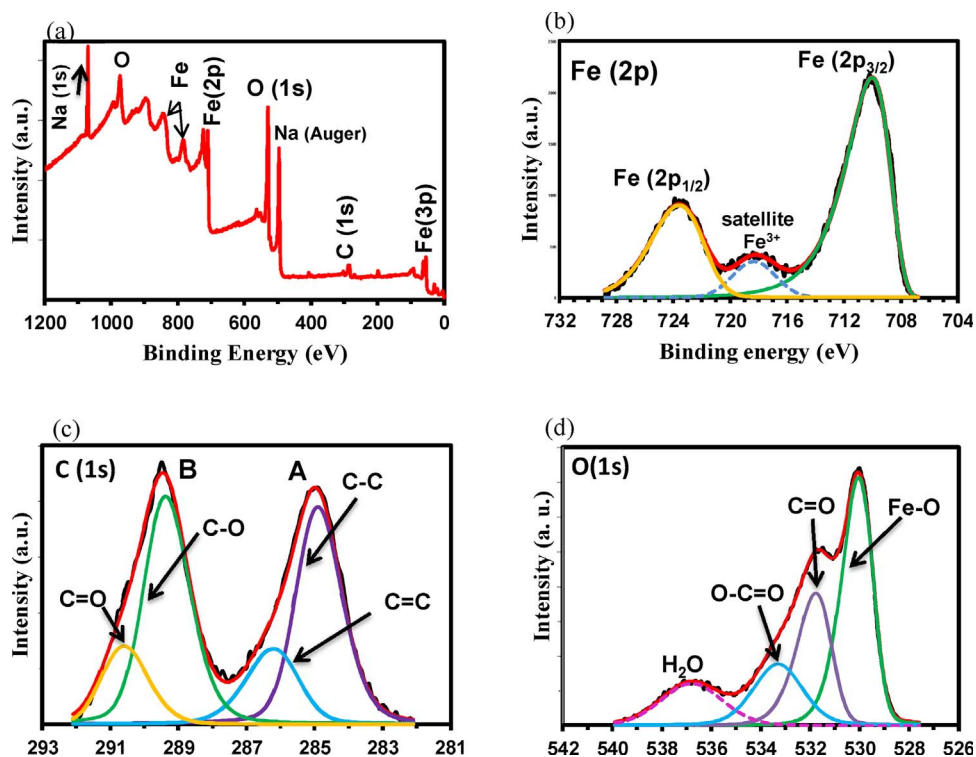


Fig. 5. (a) XPS survey spectrum of CQD@ α -Fe $_2$ O $_3$. High resolution XPS scans of Fe 2p (b), C 1s (c) and O 1s (d) core levels.

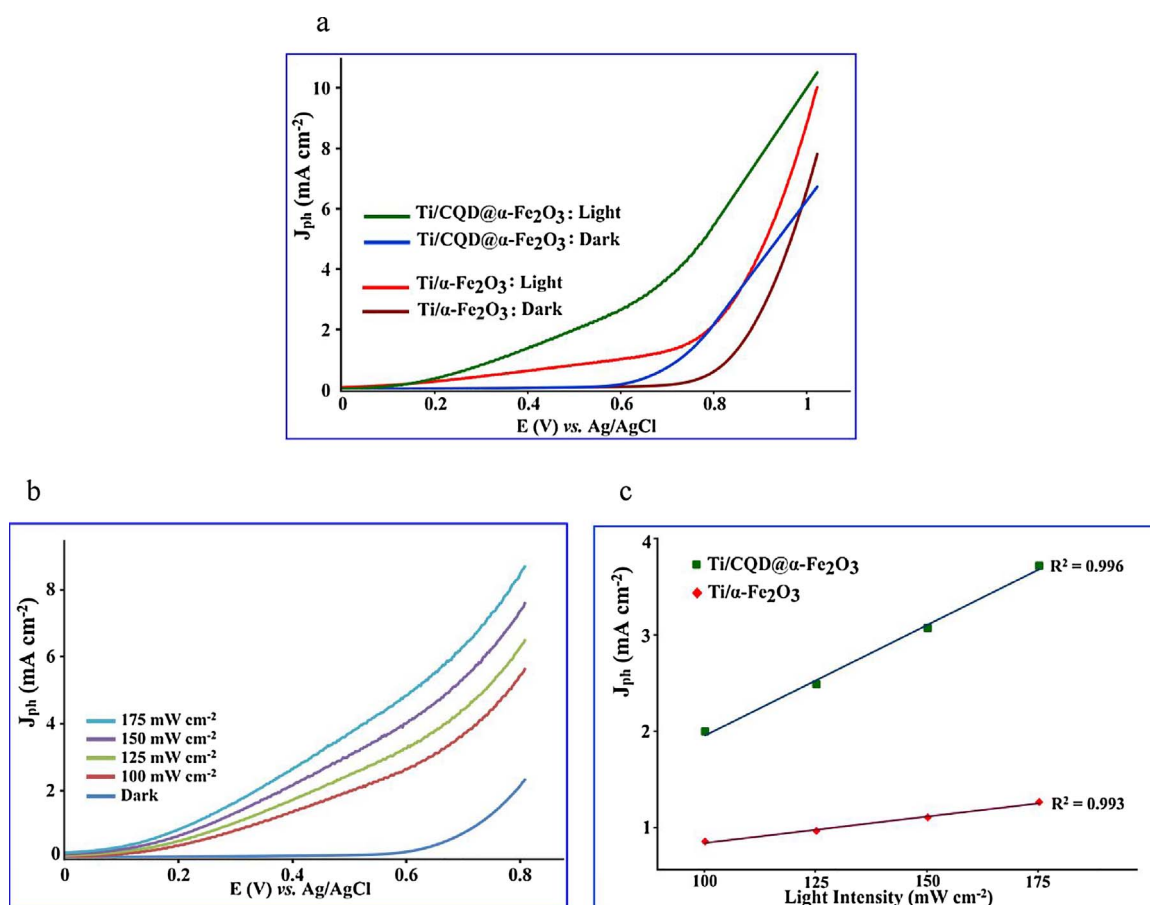
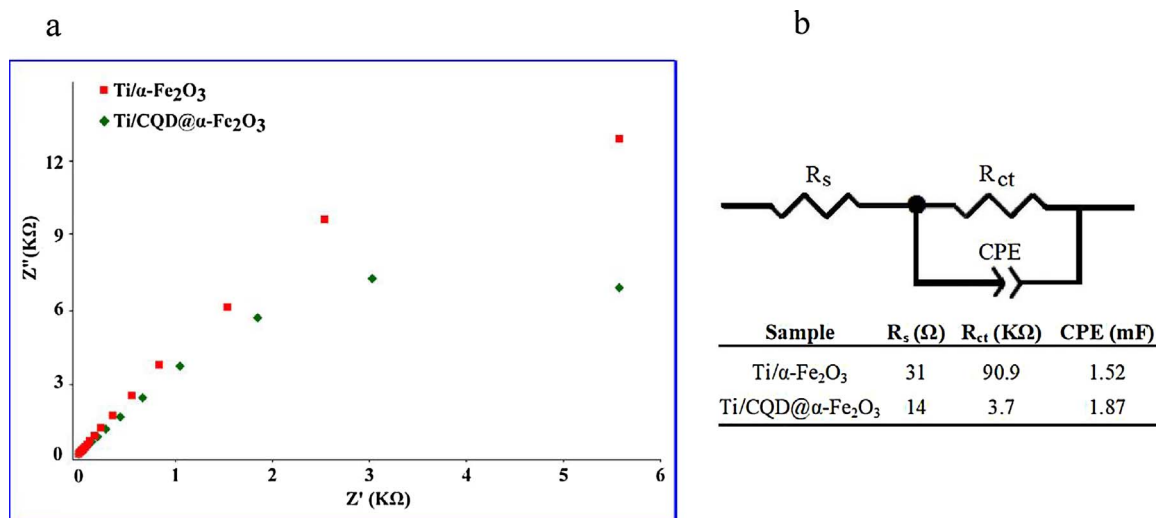


Fig. 6. (a) LSV of Ti/ α -Fe $_2$ O $_3$ and Ti/CQD@ α -Fe $_2$ O $_3$ photoanodes at the scan rate of 0.1 V s $^{-1}$, (b) LSV of Ti/CQD@ α -Fe $_2$ O $_3$ photoanode at different illumination intensities under the illumination conditions. (c) Diagram of J_{ph} versus I_{Light} at +0.5 V bias potential.

Table 2Comparison of the electrochemical and photoelectrochemical performances of Ti/CQD@ α -Fe₂O₃ photoanode with previously reported α -Fe₂O₃-based photoanodes.

Photoanode	Fabrication method	Modifier	Onset potential, E/V vs. RHE (E shift, mV)	Photocurrent density, mA cm ⁻² (E _{bias} , V)	Ref.
FTO/ α -Fe ₂ O ₃ -Co-Pi	Electron beam evaporator	Cobalt-phosphate (Co-Pi)	0.810 (–185)	1.52 (+1.50)	[36]
FTO/Sn-doped α -Fe ₂ O ₃	Hydrothermal	Doped Sn	0.80 (+150)	1.95 (+1.6)	[37]
FTO/ α -Fe ₂ O ₃ -IrO ₂ NPs	Chemical vapor deposition	IrO ₂ nanoparticles (NPs)	0.80 (–200)	3.75 (+1.23)	[38]
FTO/ α -Fe ₂ O ₃ -Co ₃ O ₄ NPs	Hydrothermal	Co ₃ O ₄ nanoparticles (NPs)	0.66 (–40)	1.20 (+1.23)	[39]
Fe/Sn-doped α -Fe ₂ O ₃	Flame annealing	Doped Sn	0.70	1.1 (+1.23)	[40]
FTO/Ti-doped α -Fe ₂ O ₃	Hydrolysis	Doped Ti	0.80 (–200)	1.83 (+1.02)	[41]
FTO/Ti-doped α -Fe ₂ O ₃	SILAR	Doped Ti	0.92 (–80)	0.85 (+1.23)	[42]
FTO/QDs- α -Fe ₂ O ₃	Hydrothermal	Hematite quantum dots	0.80 (–140)	1.60 (+1.6)	[19]
FTO/ α -Fe ₂ O ₃ /CQD	Hydrothermal	Carbon quantum dots	0.9 (–300)	0.35 (+1.23)	[43]
FTO/CDots/Co ₃ O ₄ -Fe ₂ O ₃	Hydrothermal	Carbon nanodots (CDots)-Co ₃ O ₄	0.79 (–60)	1.48 (+1.23)	[34]
ITO/C-coated α -Fe ₂ O ₃	Electrodeposition	Coated carbon	(–100)	2.1 (+0.4)	[2]
FTO/C-doped α -Fe ₂ O ₃	Magnetron sputtering	Doped carbon	–	1.18 (+0.6)	[44]
FTO/C-coated α -Fe ₂ O ₃	Pyrolysis	Coated carbon	–	2.1 (+1.23)	[45]
FTO/ α -Fe ₂ O ₃ /RGO	Hydrolysis-solvothermal	Reduced graphene oxide (RGO)	–	0.61 (+1.5)	[46]
Ti/ α -Fe ₂ O ₃	SILAR	–	0.75 (–50)	1.5 (+0.70)	This work
Ti/CQD@ α -Fe ₂ O ₃	Hydrothermal	CQDs	0.65 (–150)	2.1 (+0.70)	This work

**Fig. 7.** (a) Nyquist plots of Ti/ α -Fe₂O₃ and Ti/CQD@ α -Fe₂O₃ electrodes, (b) the equivalent circuits resulted from the data fitting by Zview.

electrochemical impedance spectroscopy (EIS) of photoanodes were measured. EIS measurements were performed in 1.0 M KOH solution at open circuit potential (V_{ocp}) with the frequency range being adjusted between 100 kHz and 0.1 Hz at the amplitude frequency of 10 mV in dark conditions. The Nyquist plots and the equivalent circuit model have been shown in Fig. 7. As it is clear, EIS equivalent circuit model for both photoelectrodes includes one sub-circuit containing a charge transfer resistance (R_{ct}) and a capacitance (RC) in parallel circuits. From the Nyquist plots and the equivalent circuits resulted from the data fitting, R_{ct} corresponding to Ti/ α -Fe₂O₃ and Ti/CQD@ α -Fe₂O₃ samples were obtained to be 90.9 K Ω and 3.7 K Ω , respectively. The main difference between Nyquist plots of these two samples is the semi-circle at higher frequencies that this part of EIS plot mainly corresponds to the e^- - h^+ recombination in bulk of photoactive material. This can be explained by the morphology differences in these two samples and their conductivities. In fact, the photo-generated e^- - h^+ pairs at the surface of CQD@ α -Fe₂O₃ nanoparticles (with the size of about 5.0 nm and lower R_{ct}) have more tendency to flow through the surface of particles compared to α -Fe₂O₃ nanorods (with the diameter of about 25 nm and higher R_{ct}). Lower R_{ct} and higher CPE values for Ti/CQD@ α -Fe₂O₃ represent improved charge transport characteristics attributed to the conductive nature of CQDs making favorable environment for charge separation in PEC reaction at the surface of Ti/CQD@ α -Fe₂O₃

nanoparticles [43,48]. So, it seems that the nanostructuring of α -Fe₂O₃ with CQDs results the faster hole transfer in bulk of material nanostructure. Consequently, significantly reduced R_{ct} and the accelerated electron transfer rate indicate a strong influence of CQDs embedded in CQD@ α -Fe₂O₃ nanostructure on the interfacial kinetics.

3.4. Photoresponsivity of Ti/ α -Fe₂O₃ and Ti/CQD@ α -Fe₂O₃ photoanodes

3.4.1. Chronoamperometry

To study the photoresponsivity of the fabricated samples, chronoamperometric technique was used at an applied E_{bias} of +0.5 V under dark and illumination conditions. Chronoamperograms of Ti/ α -Fe₂O₃ and Ti/CQD@ α -Fe₂O₃ photoanodes prepared by using hydrothermal method (4 samples) are shown in Fig. 8a. As it is clear from the results, very rapid generation of photocurrent densities (J_{ph}) was observed for all photoanodes upon visible illumination. Also, the anodic current spike is not occurred for these samples when the light is on, indicating the lack of photogenerated hole accumulation at the electrode surface because of the fast water oxidation reaction [15]. Also, the cathodic current spike was not observed when the light was off, due to the lower e^- - h^+ recombination.

As discussed, nanostructuring and crystallinity are crucial parameters affecting the photoresponsivity of hematite. To get more insight

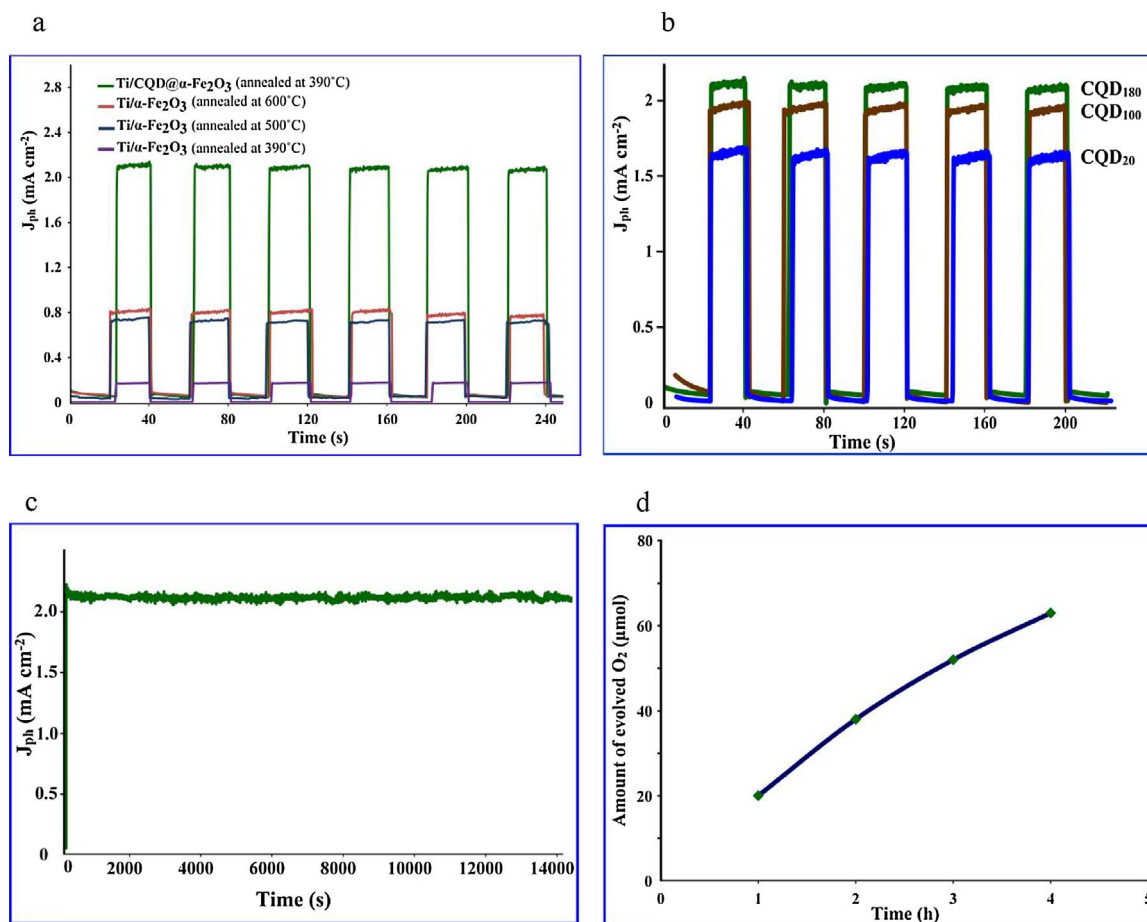


Fig. 8. (a) Photocurrent density response of Ti/α-Fe₂O₃ photoanodes annealed at 390 °C, 500 °C and 600 °C and Ti/CQD@α-Fe₂O₃ photoanode annealed at 390 °C. (b) Photoresponse of Ti/CQD@α-Fe₂O₃ samples prepared with different CQDs synthesized under the applied constant current densities of 20, 100 and 180 mA cm⁻². (c) Photoresponse of Ti/CQD@α-Fe₂O₃ under the visible light irradiation during 4 h illumination. (d) Time course of O₂ evolution from 1.0 M KOH solution with Ti/CQD@α-Fe₂O₃ photoanode under visible light irradiation. All of the experiments were performed in 1.0 M KOH at an applied bias of +0.5 V vs. Ag/AgCl.

into the effects of these two parameters on J_{ph} , we annealed Ti/α-Fe₂O₃ samples at different temperatures of 390 °C, 500 °C and 600 °C, and Ti/CQD@α-Fe₂O₃ sample at 390 °C under the air atmosphere, and studied their photoactivities. Increase in J_{ph} for three Ti/α-Fe₂O₃ samples by the increase of annealing temperature is mainly due to the improvement in crystallinity of hematite [12]. However, J_{ph} of Ti/CQD@α-Fe₂O₃ sample that was annealed at 390 °C is about 10 times higher than that of Ti/α-Fe₂O₃ sample annealed under the same temperature. This is due to the nanostructuring effect. In fact, it seems that the structure design in Ti/CQD@α-Fe₂O₃ is a significant parameter in hematite-based photoanodes to improve photoactivity. Because the average size of CQDs@α-Fe₂O₃ nanoparticulates is about 3–5 nm (Fig. 3), the proposed structure design seems to match well with the short hole-diffusion length and poor hole mobility limitations. A smaller particle size is beneficial due to the lower bulk recombination and short life time of excited holes [49].

Because of the important role of CQDs in photoresponse of hematite-based photoanodes, the effect of concentration and size of CQDs on the photocurrent density of Ti/CQDs@α-Fe₂O₃ was investigated. Beyond the optimized CQDs concentration, photocurrent density was not change drastically. To investigate the effect of size of CQDs, in the electrochemical synthesis of CQDs, various applied constant current densities were examined. At lower applied current densities, the large-sized CQDs is synthesized [20]. So, we examined various applied current densities of 20, 100 and 180 mA cm⁻² in the electrochemical synthesis of CQDs. The photoresponse of the fabricated samples have been depicted in Fig. 8b. As it is clear, increase in the size of CQDs

causes the decrease in the photoresponse of corresponding Ti/CQD@α-Fe₂O₃ photoanode. This is again indicates that the smaller particle size of CQD@α-Fe₂O₃ is beneficial due to the lower bulk recombination and short life time of excited holes.

So, the optimum photoanode is Ti/CQD@α-Fe₂O₃ with highest J_{ph} of 2.1 mA cm⁻². The stability of the sample was examined by the illumination of photoanode under the visible light irradiation and the applied bias of +0.5 V for 4 h in a tightly sealed and de-aerated 3-electrode electrochemical cell. The resulted I-t curve and the time course of O₂ evolution are shown in Fig. 8c and d, respectively. After the continuous 4 h irradiation, J_{ph} did not changed significantly ($\pm 5\%$), indicating the high stability of photoanode and tightly deposited CQDs@α-Fe₂O₃ on Ti substrate, which was confirmed by FE-SEM image of the sample after the experiment (Fig. S2).

Another possible factor affecting the photoresponsivity of α-Fe₂O₃ photoactive material is the thin film thickness. To investigate the thickness effect, we employed SILAR method. SILAR, as an alternative method to atomic layer deposition [50], is a solution-based layer-by-layer deposition method that is carried out at ambient conditions and provides tight control over thin film thickness of the resulted samples [50,51]. So, we fabricated 6 Ti/α-Fe₂O₃-n samples, where n is the cycle number of SILAR process (Table 3). Chronoamperometry was used to study the photoresponsivity of the samples at an applied E_{bias} of +0.5 V under dark and illumination conditions. The results are depicted in Fig. 9a and Table 3. As it is clear, by increase in cycle number of SILAR process (n), the photocurrent density (J_{ph}) of Ti/α-Fe₂O₃-n sample is increased from n = 10 to n = 100 and decreased in n = 150 (Fig. 9b).

Table 3

Photocurrent densities (J_{ph} , mA cm^{-2}) of six Ti/ α -Fe₂O₃ samples fabricated by using SILAR method at different number of cycles.

Sample (Ti/ α -Fe ₂ O ₃ -n)	No. of SILAR Cycles (n)	J_{ph} (mA cm^{-2})
Ti/ α -Fe ₂ O ₃ - 10	10	0.20
Ti/ α -Fe ₂ O ₃ - 20	20	0.45
Ti/ α -Fe ₂ O ₃ - 30	30	0.55
Ti/ α -Fe ₂ O ₃ - 50	50	0.65
Ti/ α -Fe ₂ O ₃ - 100	100	1.50
Ti/ α -Fe ₂ O ₃ - 150	150	1.40

The main reason for the increase in J_{ph} with increase in thin film thickness is the increase in light absorption by thicker photoactive material deposited on Ti substrate. The decline at Ti/ α -Fe₂O₃-150 sample seems to be from the short hole-diffusion length as an important limiting factor [4] and the limitations in charge separation [50].

It should be noted that J_{ph} of optimized Ti/ α -Fe₂O₃-100 sample fabricated by SILAR method (with J_{ph} of 1.50 mA cm^{-2}) is about 2 times higher than that of optimized Ti/ α -Fe₂O₃-L6h sample prepared by hydrothermal method (with J_{ph} of 0.8 mA cm^{-2}). This can be explained by the effect of thickness of α -Fe₂O₃ deposited on substrate. The average thicknesses of Ti/ α -Fe₂O₃-L6h and Ti/ α -Fe₂O₃-100 samples are $\sim 100 \text{ nm}$ and $\sim 50 \text{ nm}$, respectively, obtained from cross-section FE-SEM images (Figs. S1 and S3). So, from these findings, it seems that the film thickness is a crucial factor that should be controlled in the fabrication of α -Fe₂O₃-based photoanodes. Finally, although the surface morphology of Ti/ α -Fe₂O₃-100 and Ti/CQD@ α -Fe₂O₃ samples are the nanoparticles deposited on Ti substrate, J_{ph} of Ti/CQD@ α -Fe₂O₃ sample annealed at 390°C (with J_{ph} of 2.10 mA cm^{-2}) is about 8 times higher than that of Ti/ α -Fe₂O₃-100 and 10 times higher than that of Ti/ α -Fe₂O₃-L6h sample annealed at the same conditions. This is mainly due to the crucial effect of CQDs with the optimized size in the range of 1.5–3 nm acting as nano-scaffolds for the growth of CQD@ α -Fe₂O₃ nanoparticulates having higher charge transfer rate and short paths for hole transport.

3.4.2. Chronopotentiometry

Open-circuit photovoltage (V_{oc}) decay measurements were employed by using chronopotentiometry to investigate the charge collection properties of Ti/ α -Fe₂O₃ and Ti/CQD@ α -Fe₂O₃ samples. The samples were exposed to visible light irradiation for a constant time of 75 s before turning off the light. Transient values of the open-circuit potential (V_{oc}) were measured as a function of time for 150 s after the illumination was turned off. The chronopotentiograms are shown in Fig. 10a. As it is clear, the photo-potential of Ti/CQD@ α -Fe₂O₃ is lower than that of Ti/ α -Fe₂O₃ photoanode, indicating that the free electron

density is increased in CQD@ α -Fe₂O₃ under similar illumination condition [47]. So, there are more photoelectrons accumulated on the surface of Ti/CQD@ α -Fe₂O₃ compared to Ti/ α -Fe₂O₃. As Fig. 10a shows, under the illumination, the Fermi level of two samples is negatively shifted and when the light is off, the photo-generated charges leak out of the substrate. Open-circuit voltage (V_{oc}) values for Ti/CQD@ α -Fe₂O₃ and Ti/ α -Fe₂O₃ samples are -0.31 V and -0.21 V , respectively. The electron life time (τ_n) can be calculated from chronopotentiograms using the following equation [52]:

$$\tau_n = \frac{k_B T}{e} \left(\frac{dV_{oc}}{dt} \right)^{-1} \quad (1)$$

where k_B , T and e are the Boltzmann constant, temperature (in K) and charge of electron, respectively. τ_n for Ti/CQD@ α -Fe₂O₃ and Ti/ α -Fe₂O₃ samples were calculated to be 240 and 110 ms, respectively. So, the photo-generated carrier life time is increased in CQD@ α -Fe₂O₃.

The band structure of photoactive CQD@ α -Fe₂O₃ is schematically represented in Fig. 10b. As confirmed by HRTEM images (Fig. 3e), at CQD@ α -Fe₂O₃ nanoparticulates, CQDs act as core for the growth of α -Fe₂O₃ shell. So, by the irradiation of CQD@ α -Fe₂O₃, α -Fe₂O₃ shell will act as light absorber material. In fact, this is the main reason that the energy band gaps of Ti/ α -Fe₂O₃ and Ti/CQD@ α -Fe₂O₃ are almost the same (Fig. 4b and c). In the other hand, the results of chronopotentiometric technique showed that the photopotential of Ti/CQD@ α -Fe₂O₃ is lower than that of Ti/ α -Fe₂O₃ photoanode, indicating that the free electron density is increased in CQD@ α -Fe₂O₃ under similar illumination condition. In both of photoanodes (n-type semiconductors) the electrons are the majority carriers and holes are the minority carriers. So, under the illumination conditions, there are more photoelectrons accumulated on the surface of Ti/CQD@ α -Fe₂O₃ compared to Ti/ α -Fe₂O₃, and Ti/CQD@ α -Fe₂O₃ has higher donor density and enhanced electron density. In fact, under the illumination, the Fermi level of Ti/CQD@ α -Fe₂O₃ sample is more negatively shifted compare to Ti/ α -Fe₂O₃. More negative open circuit potential (V_{oc}) and higher electron life time (τ_n) for Ti/CQD@ α -Fe₂O₃ indicate that the minority carrier (h^+) accumulation and e^- - h^+ recombination is reduced at the surface of Ti/CQD@ α -Fe₂O₃ sample. The probable mechanism for describing the enhanced photoactivity CQD@ α -Fe₂O₃ compared to α -Fe₂O₃ is the h^+ transfer (or h^+ hopping) from valence band (VB) of α -Fe₂O₃ to the HOMO of CQDs (Fig. 10b).

Careful curve fitting of high resolution XPS data revealed that C–O bonds are attributed to chemical bond between carbon and oxygen atoms of CQDs and α -Fe₂O₃. Thus, the hole transfer between CQDs and α -Fe₂O₃ is more feasible. Because of the short hole-diffusion length in the structure of α -Fe₂O₃, nanostructuring by CQD (which was confirmed by HRTEM in this work) causes the faster hole transportation by

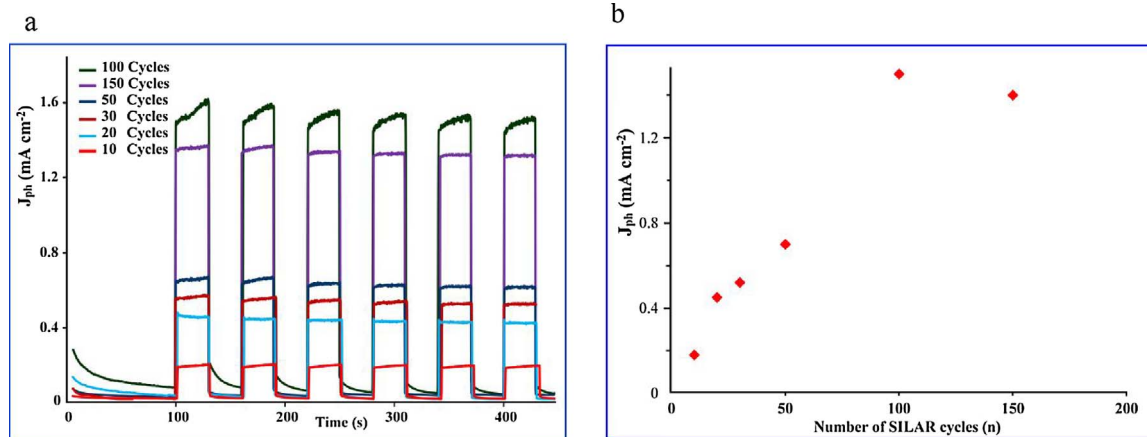


Fig. 9. (a) Photoresponse of Ti/ α -Fe₂O₃-n photoanodes fabricated by SILAR method at different SILAR cycles of 10, 20, 30, 50, 100 and 150 cycles and annealed at 500°C . (b) Photocurrent density of Ti/ α -Fe₂O₃-n as a function of SILAR cycles (n).

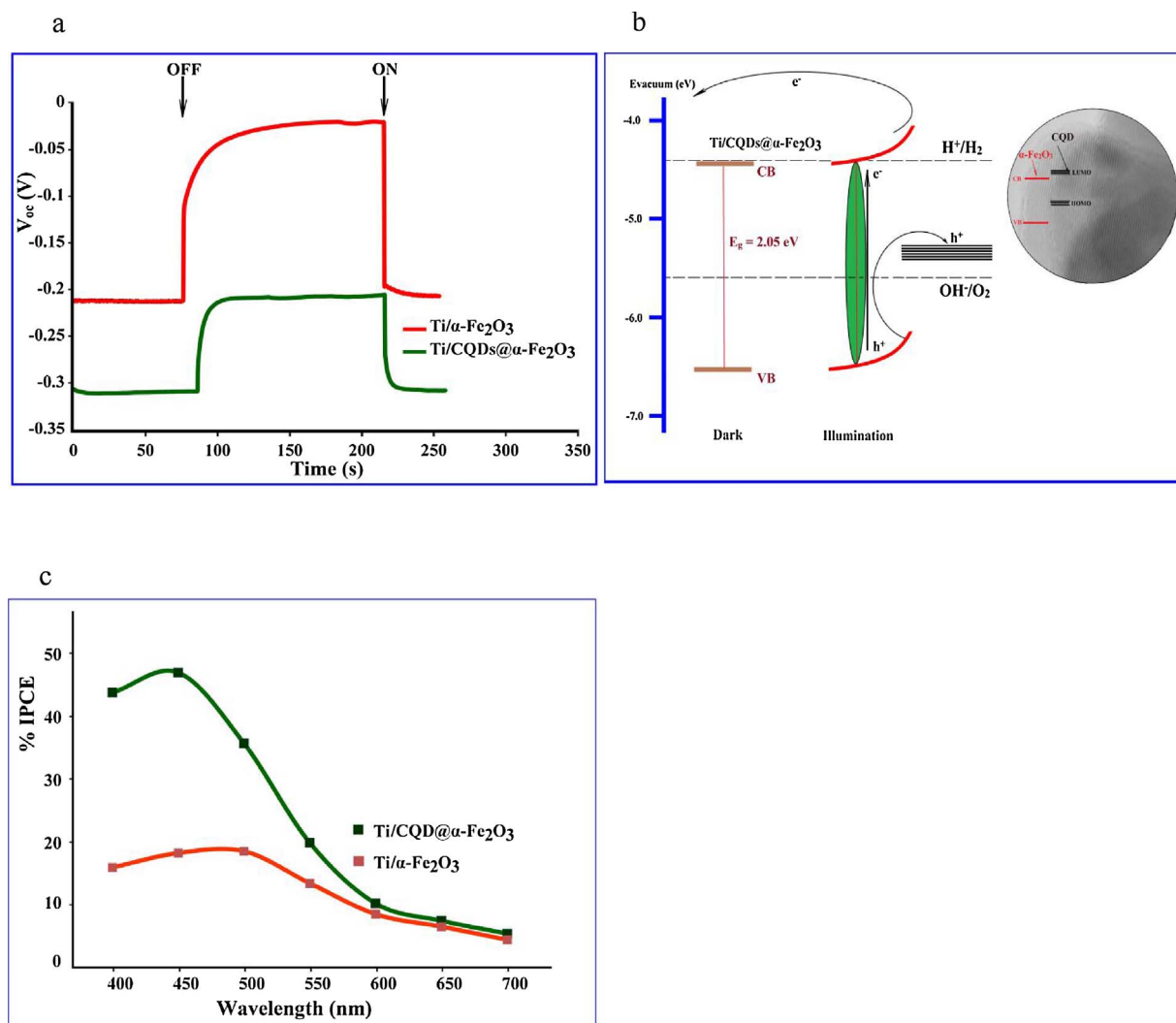


Fig. 10. (a) Open circuit photo-voltage in light on-off process for $Ti/\alpha-Fe_2O_3$ and $Ti/CQD@α-Fe_2O_3$ samples. (b) Schematic diagram for band structure of $CQD@α-Fe_2O_3$ and the possible mechanism of e^- - h^+ transfer in illuminated photoanode. (c) %IPCE of the samples versus irradiated wavelength (nm) under constant illumination intensity (100 mW cm^{-2}).

CQDs in $CQD@α-Fe_2O_3$ and reduces the e^- - h^+ recombination. So, h^+ hopping from the VB of $α-Fe_2O_3$ to HOMO CQDs can be expected.

3.4.3. IPCE measurement

To investigate the change in photo-response of the $Ti/CQD@α-Fe_2O_3$ and $Ti/\alpha-Fe_2O_3$ samples thin films as a function of the irradiation wavelengths (λ), Incident photon-to-current efficiency (IPCE) or action spectra of these two samples was measured using the following relation [53]:

$$\%IPEC = \frac{hc}{e} \frac{J(\text{mA} \cdot \text{cm}^{-2})}{\lambda(\text{nm})P(\text{mW} \cdot \text{cm}^{-2})} \times 100 \quad (2)$$

where, J_{ph} and P are the photocurrent density and the intensity of illuminating light at each wavelength, respectively. The obtained results are shown in Fig. 10c. The IPCE's results are in agreement with the chronoamperometric results.

4. Conclusions

An appropriate approach for the fabrication of hematite-based photoanode with high photocurrent density is the structure design with nanostructured morphology. So, in this respect, $Ti/CQD@α-Fe_2O_3$ photoanode was proposed because of the suppressed electron-hole recombination, higher charge transfer rate and faster water oxidation

kinetics at the surface of photoelectrode.

Acknowledgement

The authors would like to thank Research Council of Alzahra University for financial support.

Appendix A. Supplementary data

Supplementary data associated with this article can be found, in the online version, at <https://doi.org/10.1016/j.apcatb.2018.01.016>.

References

- [1] H. Gao, C. Liu, H.E. Jeong, P. Yang, Plasmon-enhanced photocatalytic activity of iron oxide on gold nanopillars, *ACS Nano* 6 (2012) 234–240.
- [2] T.H. Wang, Y.N. Chen, C.C. Chiang, Y.K. Hsieh, P.C. Li, C.F. Wang, Carbon-coated hematite electrodes with enhanced photoelectrochemical performance obtained through an electrodeposition method with a citric acid additive, *ChemElectroChem* 3 (2016) 966–975.
- [3] C. Li, T. Wang, Z. Luo, S. Liu, J. Gong, Enhanced charge separation through ALD-modified Fe_2O_3/Fe_2TiO_5 nanorod heterojunction for photoelectrochemical water oxidation, *Small* 12 (2016) 3415–3422.
- [4] Y. Lin, G. Yuan, S. Sheehan, S. Zhou, D. Wang, Hematite-based solar water splitting: challenges and opportunities, *Energy Environ. Sci.* 4 (2011) 4862–4869.
- [5] J. Wang, J. Yang, Z. Zheng, T. Lu, W. Gao, The role of thin NiPi film for enhancing solar water splitting performance of Ti doped hematite, *Appl. Catal. B: Environ.* 218

- (2017) 277–286.
- [6] M.W. Kanan, D.G. Nocera, In situ formation of an oxygen-evolving catalyst in neutral water containing phosphate and Co^{2+} , *Science* 321 (2008) 1072–1075.
 - [7] B. Klahr, S. Gimenez, F. Fabregat-Santiago, J. Bisquert, T.W. Hamann, Photoelectrochemical and impedance spectroscopic investigation of water oxidation with Co-Pi-coated hematite electrodes, *J. Am. Chem. Soc.* 134 (2012) 16693–16700.
 - [8] T.H. Wang, H.T. Hung, Y.R. Cheng, M.C. Huang, Y.K. Hsieh, C.F. Wang, Understanding the role of phosphate in the photoelectrochemical performance of cobalt phosphate/hematite electrode systems, *RSC Adv.* 6 (2016) 28236–28247.
 - [9] W. Li, S.W. Sheehan, D. He, Y. He, X. Yao, R.L. Grimm, G.W. Brudvig, D. Wang, Hematite-based solar water splitting in acidic solutions: functionalization by mono- and multilayers of iridium oxygen-evolution catalysts, *Angew. Chem. Int. Ed.* 54 (2015) 11428–11432.
 - [10] F.L. Forman, N. Tetreault, M. Cornuz, T. Moehl, M. Gratzel, K. Sivula, Passivating surface states on water splitting hematite photoanodes with alumina overlayers, *Chem. Sci.* 2 (2011) 737–743.
 - [11] A. Cots, R. Gómez, Ytterbium modification of pristine and molybdenum-modified hematite electrodes as a strategy for efficient water splitting photoanodes, *Appl. Catal. B: Environ.* 219 (2017) 492–500.
 - [12] J.Y. Kim, G. Magesh, D.H. Youn, J.W. Jang, J. Kubota, K. Domen, J.S. Lee, Single-crystalline, wormlike hematite photoanodes for efficient solar water splitting, *Sci. Rep.* 3 (2013) 2681.
 - [13] I. Kondofersky, H. Dunn, A. Muller, B. Mandlmeier, J.M. Feckl, D. Fattakhova-Rohlfing, C. Scheu, L.M. Peter, T. Bein, Electron collection in host-guest nanostructured hematite photoanodes for water splitting: the influence of scaffold doping density, *ACS Appl. Mater. Interfaces* 7 (2015) 4623–4630.
 - [14] O. Zandi, A.R. Schon, H. Hajibabaei, T.W. Hamann, Enhanced charge separation and collection in high performance electrodeposited hematite films, *Chem. Mater.* 28 (2016) 765–771.
 - [15] M. Zhang, W. Luo, N. Zhang, Z. Li, T. Yu, Z. Zou, A facile strategy to passivate surface states on the undoped hematite photoanode for water splitting, *Electrochem. Commun.* 23 (2012) 41–43.
 - [16] A. Annamalai, A. Subramanian, U. Kang, H. Park, S.H. Choi, J.S. Jang, Activation of hematite photoanodes for solar water splitting: effect of FTO deformation, *J. Phys. Chem. C* 119 (2015) 3810–3817.
 - [17] C.H. Bak, K. Kim, K. Jung, J.B. Kim, J.H. Jang, Efficient photoelectrochemical water splitting of nanostructured hematite on a three-dimensional nanoporous metal electrode, *J. Mater. Chem. A* 2 (2014) 17249–17252.
 - [18] M.G. Ahmed, T.A. Kandiel, A.Y. Ahmed, I. Kretschmer, F. Rashwan, D. Bahnemann, Enhanced photoelectrochemical water oxidation on hematite photoanode via p- CaFe_2O_4 /n- Fe_2O_3 heterojunction formation, *J. Phys. Chem. C* 119 (2015) 5864–5871.
 - [19] Z. Hu, Z. Shen, J.C. Yu, F. Cheng, Intrinsic defect based homojunction: a novel quantum dots photoanode with enhanced charge transfer kinetics, *Appl. Catal. B: Environ.* 203 (2017) 829–838.
 - [20] H.T. Li, X.D. He, Z.H. Kang, H. Huang, Y. Liu, J.L. Liu, S.Y. Lian, C.H.A. Tsang, X.B. Yang, S.T. Lee, Water soluble fluorescent carbon quantum dots and photocatalyst design, *Angew. Chem. Int. Ed.* 49 (2010) 4430–4434.
 - [21] O. Moradlou, N. Tedadi, A. Banazadeh, N. Naseri, Effect of RGO/ $\text{Zn}_3\text{Cd}_{1-x}\text{S}$ crystalline phase on solar photoactivation processes, *RSC Adv.* 6 (2016) 46282–46290.
 - [22] J.K. Bailey, C.J. Brinker, M.L. Mecartney, Growth mechanisms of iron oxide particles of differing morphologies from the forced hydrolysis of ferric chloride solutions, *J. Colloid Interface Sci.* 157 (1993) 1–13.
 - [23] O.V. Kharisova, B.I. Kharisov, Variations of interlayer spacing in carbon nanotubes, *RSC Adv.* 4 (2014) 30807–30815.
 - [24] N. Iwashita, C.R. Park, H. Fujimoto, M. Shiraishi, M. Inagaki, Specification for a standard procedure of X-ray diffraction measurements on carbon materials, *Carbon* 42 (2004) 701–714.
 - [25] K. Schulz, R. Schmack, H.W. Klemm, A. Kabelitz, T. Schmidt, F. Emmerling, R. Kraehnert, Mechanism and kinetics of hematite crystallization in air: linking bulk and surface models via mesoporous films with defined nanostructure, *Chem. Mater.* 29 (2017) 1724–1734.
 - [26] A.K. Patra, S.K. Kundu, A. Bhaumik, D. Kim, Morphology evolution of single-crystalline hematite nanocrystals: magnetically recoverable nanocatalysts for enhanced facet-driven photoredox activity, *Nanoscale* 8 (2016) 365–377.
 - [27] B.Y. Yu, S.Y. Kwak, Carbon quantum dots embedded with mesoporous hematite nanospheres as efficient visible light-active photocatalysts, *J. Mater. Chem.* 22 (2012) 8345–8353.
 - [28] Y. Luo, J. Luo, J. Jiang, W. Zhou, H. Yang, X. Qi, H. Zhang, H.J. Fan, D.Y.W. Yu, C.M. Li, T. Yu, Seed-assisted synthesis of highly ordered TiO_2 @ $\alpha\text{-Fe}_2\text{O}_3$ core/shell arrays on carbon textiles for lithium-ion battery applications, *Energy Environ. Sci.* 5 (2012) 6559–6566.
 - [29] Y. Li, C. Zhu, T. Lu, Z. Guo, D. Zhang, J. Ma, S. Zhu, Simple fabrication of $\alpha\text{-Fe}_2\text{O}_3$ /carbon composite for use in a high-performance lithium ion battery, *Carbon* 52 (2013) 565–573.
 - [30] X. Hu, J.C. Yu, J. Gong, Q. Li, G. Li, $\alpha\text{-Fe}_2\text{O}_3$ nanorings prepared by a microwave-assisted hydrothermal process and their sensing properties, *Adv. Mater.* 19 (2007) 2324–2329.
 - [31] L.L. Li, J. Ji, R. Fei, C.Z. Wang, Q. Lu, J.R. Zhang, L.P. Jiang, J.J. Zhu, A facile microwave avenue to electrochemiluminescent two-color graphene quantum dots, *Adv. Funct. Mater.* 22 (2012) 2971–2979.
 - [32] H. Yu, Y. Zhao, C. Zhou, L. Shang, Y. Peng, Y. Cao, L.Z. Wu, C.H. Tung, T. Zhang, Carbon quantum dots/ TiO_2 composites for efficient photocatalytic hydrogen evolution, *J. Mater. Chem. A* 2 (2014) 3344–3351.
 - [33] J. Heuer, J. Stubbs, An XPS characterization of FeCO_3 films from CO_2 corrosion, *Corros. Sci.* 41 (1999) 1231–1243.
 - [34] P. Zhang, T. Wang, X. Chang, L. Zhang, J. Gong, Synergistic cocatalytic effect of carbon nanodots and Co_3O_4 nanoclusters for the photoelectrochemical water oxidation on hematite, *Angew. Chem. Int. Ed.* 55 (2016) 5851–5855.
 - [35] J.Y. Kim, J.W. Jang, D.H. Youn, J.Y. Kim, E.S. Kim, J.S. Lee, Graphene-carbon nanotube composite as an effective conducting scaffold to enhance the photoelectrochemical water oxidation activity of a hematite film, *RSC Adv.* 2 (2012) 9415–9422.
 - [36] B. Eftekhari, A. Moshaii, A. Dabirian, N. Sobhkhiz Vayghan, Optimization of charge transport in a Co-Pi modified hematite thin film produced by scalable electron beam evaporation for photoelectrochemical water oxidation, *J. Mater. Chem. A* 5 (2017) 3412–3424.
 - [37] Y. Ling, G. Wang, D.A. Wheeler, J.Z. Zhang, Y. Li, Sn-doped hematite nanostructures for photoelectrochemical water splitting, *Nano Lett.* 11 (2011) 2119–2125.
 - [38] S.D. Tilley, M. Cornuz, K. Sivula, M. Gratzel, Light-induced water splitting with hematite: improved nanostructure and iridium oxide catalysis, *Angew. Chem.* 122 (2010) 6549–6552.
 - [39] L. Xi, P.D. Tran, S.Y. Chiam, P.S. Bassi, W.F. Mak, H.K. Mulmudi, S.K. Batabyal, J. Barber, J.S.C. Loo, L.H. Wong, Co_3O_4 -decorated hematite nanorods as an effective photoanode for solar water oxidation, *J. Phys. Chem. C* 116 (2012) 13884–13889.
 - [40] L. Wang, C.Y. Lee, A. Mazare, K. Lee, J. Muller, E. Spiecker, P. Schmuki, Enhancing the water splitting efficiency of Sn-doped hematite nanoflakes by flame annealing, *Chem. Eur. J.* 20 (2014) 77–82.
 - [41] G. Wang, Y. Ling, D.A. Wheeler, K.E.N. George, K. Horsley, C. Heske, J.Z. Zhang, Y. Li, Facile synthesis of highly photoactive $\alpha\text{-Fe}_2\text{O}_3$ -based films for water oxidation, *Nano Lett.* 11 (2011) 3503–3509.
 - [42] A.J. Abel, A.M. Patel, S.Y. Smolin, B. Opananont, J.B. Baxter, Enhanced photoelectrochemical water splitting via SILAR-deposited Ti-doped hematite thin films with an FeOOH overlayer, *J. Mater. Chem. A* 4 (2016) 6495–6504.
 - [43] L. Li, C. Liu, Y. Qiu, N. Mitsuzak, Z. Chen, Convex-nanorods of $\alpha\text{-Fe}_2\text{O}_3$ /CQDs heterojunction photoanode synthesized by a facile hydrothermal method for highly efficient water oxidation, *Int. J. Hydrog. Energy* 42 (2017) 19654–19663.
 - [44] M.C. Huang, W.S. Chang, J.C. Lin, Y.H. Chang, C.C. Wu, Magnetron sputtering process of carbon-doped $\alpha\text{-Fe}_2\text{O}_3$ thin films for photoelectrochemical water splitting, *J. Alloy Compd.* 636 (2015) 176–182.
 - [45] J. Deng, X. Lv, J. Gao, A. Pu, M. Li, X. Sun, J. Zhong, Facile synthesis of carbon-coated hematite nanostructures for solar water splitting, *Energy Environ. Sci.* 6 (2013) 1965–1970.
 - [46] Q. Wu, J. Zhao, K. Liu, H. Wang, Z. Sun, P. Li, S. Xue, Ultrathin hematite film for photoelectrochemical water splitting enhanced with reducing graphene oxide, *Int. J. Hydrog. Energy* 40 (2015) 6763–6770.
 - [47] M. Qorbani, N. Naseri, O. Moradlou, R. Azimirad, A.Z. Moshfegh, How CdS nanoparticles can influence TiO_2 nanotube arrays in solar energy applications, *Appl. Catal. B: Environ.* 162 (2015) 210–216.
 - [48] J.Y. Kim, H. Jun, S.J. Hong, H.G. Kim, J.S. Lee, Charge transfer in iron oxide photoanode modified with carbon nanotubes for photoelectrochemical water oxidation: an electrochemical impedance study, *Int. J. Hydrog. Energy* 36 (2011) 9462–9468.
 - [49] L. Wang, C.Y. Lee, P. Schmuki, Ti and Sn co-doped anodic $\alpha\text{-Fe}_2\text{O}_3$ films for efficient water splitting, *Electrochem. Commun.* 30 (2013) 21–25.
 - [50] A.J. Abel, I. Garcia-Torregrosa, A.M. Patel, B. Opananont, J.B. Baxter, *J. Phys. Chem. C* 119 (2015) 4454–4465.
 - [51] M. Zirak, O. Moradlou, M.R. Bayati, Y.T. Nien, A.Z. Moshfegh, On the growth and photocatalytic activity of the vertically aligned ZnO nanorods grafted by CdS shells, *Appl. Surf. Sci.* 273 (2013) 391–398.
 - [52] A. Zaban, M. Greenshtein, J. Bisquert, Determination of the electron lifetime in nanocrystalline dye solar cells by open-circuit voltage decay measurements, *ChemPhysChem* 4 (2003) 859–864.
 - [53] B. Alotaibi, H.P.T. Nguyen, S. Zhao, M.G. Kibria, S. Fan, Z. Mi, Highly stable photoelectrochemical water splitting and hydrogen generation using a double-band InGaN/GaN core/shell nanowire photoanode, *Nano Lett.* 13 (2013) 4356–4361.